SCIENCE CHINA
Technological Sciences

•Article•

August 2018 Vol.61 No. 8: 1217–1227
https://doi.org/10.1007/s11431-017-9171-x

Prediction of preferential fluid flow in porous structures based on topological network models: Algorithm and experimental validation

JU Yang[1,2,3*], LIU Peng[1,4], ZHANG DongShuang[5], DONG JiaBin[2], RANJITH P. G.[6] & CHANG Chun[1,3]

[1] *State Key Laboratory of Coal Resources and Safe Mining, China University of Mining and Technology, Beijing 100083, China;*
[2] *State Key Laboratory for Geomechanics and Deep Underground Engineering, China University of Mining and Technology, Xuzhou 221116, China;*
[3] *School of Mechanics and Civil Engineering, China University of Mining & Technology, Beijing 100083, China;*
[4] *School of Resources and Safety Engineering, China University of Mining & Technology, Beijing 100083, China;*
[5] *Institute of Mechanics, Chinese Academy of Science, Beijing 100190, China;*
[6] *Department of Civil Engineering, Monash University, Melbourne, Victoria 3800, Australia*

Received August 12, 2017; accepted October 30, 2017; published online February 1, 2018

The understanding and prediction of preferential fluid flow in porous media have attracted considerable attention in various engineering fields because of the implications of such flows in leading to a non-equilibrium fluid flow in the subsurface. In this study, a novel algorithm is proposed to predict preferential flow paths based on the topologically equivalent network of a porous structure and the flow resistance of flow paths. The equivalent flow network was constructed using Poiseuille's law and the maximal inscribed sphere algorithm. The flow resistance of each path was then determined based on Darcy's law. It was determined that fluid tends to follow paths with lower flow resistance. A computer program was developed and applied to an actual porous structure. To validate the algorithm and program, we tested and recorded two-dimensional (2D) water flow using an ablated Perspex sheet featuring the same porous structure investigated using the analytical calculations. The results show that the measured preferential flow paths are consistent with the predictions.

preferential flow, porous structure, topological networks, flow resistance, Darcy's law, experimental validation

Citation: Ju Y, Liu P, Zhang D S, et al. Prediction of preferential fluid flow in porous structures based on topological network models: Algorithm and experimental validation. Sci China Tech Sci, 2018, 61: 1217–1227, https://doi.org/10.1007/s11431-017-9171-x

1 Introduction

A non-equilibrium flow in a porous medium may generate preferential flow, which is a significant transport mechanism [1]. This phenomenon is relevant to many engineering applications, ranging from the extraction of oil and gas to the transport of contaminants in soil and aquifers, and has the following implications: 1) the existence of preferential flow paths leads to inefficient cyclic water flooding, which reduces oil recovery efficiency in reservoirs [2]; and 2) with regard to watershed and contaminant management, preferential flow reduces solute residence time, which allows for degradation in the soil, and thereby increases the risk of agrochemical pollution [3,4]. The mechanisms that contribute to preferential flow are typically caused by destabilization of the wetting front [5], which is significantly enhanced by textural heterogeneities [6]. Inter-aggregate pores, shrinkage fractures, and fissures all make a porous

*Corresponding author (email: juy@cumtb.edu.cn)

medium more heterogeneous and cause local differences in hydraulic conductivity. Consequently, geological heterogeneity of the pore structure is frequently a prominent factor governing fluid flow behavior [7]. As water flows into the porous structure, the sharp contrast in pore size and tortuosity relative to the surrounding textural pores leads to an abrupt increase in the water flow rate with only a small increase in water pressure [8]. Understanding the relation between flow properties and the heterogeneous structure of a porous medium is crucial for predicting preferential flow paths.

One essential approach to investigate multiple fluid transformation is to monitor the dynamic fluid flow process through porous structures etched into a transparent material [9,10]. Such micro-models are advantageous because they enable fluid flow trajectories to be captured using a camera. A dye tracer is added to the fluid to enhance the contrast between the fluid and solid and identify flow paths [11,12]. Additionally, non-destructive imaging (including X-ray CT scanning, electrical resistance tomography (ERT), radar, and ultrasound techniques) has facilitated the study of flow structure within porous media [13]. X-ray CT scanning enables the creation of three-dimensional (3D) visualizations of preferential paths, which can elucidate fluid behavior in porous structures [14–16]. However, this method depends on the quality of the CT system and generally has certain limitations in sample size. Both ERT and radar techniques can be applied to larger cores and in the field to demonstrate water movement [17–20].

One step toward modeling the heterogeneity of a porous structure is to develop non-equilibrium flow models. Evidence at the pore scale has shown that two primary factors control the hydraulic properties of a porous structure: the pore size distribution and the topology of the pore space (which reflects the nature of pore interconnection). Topological properties have been demonstrated to have greater contributions to the hydraulic conductivity of a porous medium than does pore size alone [21–24]. A promising approach to predicting fluid flow in a complex porous structure is to use network models that represent the topological features of a porous medium. Development of pore network models (PNMs) based on real rock structures has improved topological partitions of the pore space and fluid transport predictions based on CT data [25,26]. Additional methods have been developed based on genetic algorithms [27] or calculating the fluid conductance of network elements by applying lattice Boltzmann (LB) or computational fluid dynamics (CFD) algorithms to the sub-volumes defined by each separate network element [28,29].

A useful method for extracting a pore network is to directly measure the geometrical characteristics of pore morphology using undisturbed samples [30,31]. A porous structure consists of pores and throats. Pores represent large empty spaces and are connected through narrow throats. Therefore, the nodes in the network are always pores [32,33]. The skeleton of a porous structure is extracted to compose a topological network indicating the connectivity of pores and throats [34]. Moreover, topological properties can be interpreted based on image processing. In a study of hydraulic properties, Vogel et al. [35–37] proposed a connectivity function defined using a 3D Euler number to represent the spatial connectivity of pores. In addition, Deurer et al. [38] identified a flow path network by spatially linking the scaling factors of the water-retention curves. Yang et al. [39] suggested using graph theory to determine the preferential paths in a network model. Based on the previous studies cited above, it can be concluded that at the pore scale, topological characteristic is an important factor affecting preferential flow, and can be represented well using a single network model [40]. However, it is still difficult to apply and verify the preferential flow model in actual porous structures.

The purpose of this study is to develop an algorithm for predicting the preferential paths of a fluid flow, depending on the equivalent pore network model that represents the actual topological properties of porous structures based on graph theory. The methods used to extract the equivalent pore network were developed from the existing graph theory and are briefly discussed herein. The hypothesis is that all fluid flows will first select paths with the lowest flow resistance during transport, which are defined as the preferential paths. The flow resistance of each path is determined based on Darcy's law. Our experiments verify that a fluid prefers to follow paths with lower flow resistance. A computer program has been developed to determine the preferential flow paths of an actual porous structure. The focus of this paper is describing a method that can be applied to a complex porous medium, and verifying the applied algorithm by experimentally capturing the fluid flow process within the same porous structure.

2 Determination of preferential flow paths based on pore network model

2.1 Pore network modeling

The network model is able to simulate fluid flow directly in pore-scale images. It has been demonstrated that flow and transport can be computed directly onto the image of either a 3D representative pore space or a topologically equivalent network. To extract a pore network, a skeleton is acquired through integration of the maximal inscribed sphere and the grassfire algorithm. This skeleton, which is the medial axis of the porous structure, has the same topological and geometric properties as the porous structure [41,42]. In this paper, the maximal inscribed sphere algorithm [43,44] is coupled with the grassfire algorithm [45,46] to extract the

skeleton from a pore space image. The general procedure is briefly described below:

1) Searching voids and matrix. Black pixels are initially picked out by traversing the binary image, and denoted as set S_{void}, whereas the remaining white pixels are denoted as set S_{matrix}. Because the interface of a matrix and void is also the boundary of S_{void} or S_{matrix}, pixels belonging to S_{matrix} and connected to black pixels are specified as interface set ∂_{s}.

2) Computing the maximal inscribed circles. The minimal distance from any pixel in S_{void} to ∂_{s} is calculated based on the Euclidean distance between two points v_i and v_j (eq. (1)). Consequently, the radius of the maximal inscribed circle is calculated for each pixel belonging to S_{void}, as shown in Figure 1. The radius of the circle is defined as the corresponding radius of the pixel and is denoted as r_i (eq. (2)) [42,47]. For pixels belonging to S_{matrix}, r_i is evaluated as zero.

$$\text{dist}(v_i, v_j) = \sqrt{(x_i - x_j)^2 + \left(y_i - y_j\right)^2}, \tag{1}$$

$$r_i = \min\left\{\text{dist}(v_i, v_j) \,\middle|\, v_i \in S_{\text{void}}, v_j \in \partial_{\text{s}}\right\}. \tag{2}$$

3) Discriminating the porous body. The center of the porous body must be a component of the skeleton, and these pixels therefore cannot be omitted. Because a porous body normally occupies the largest r_i in its neighborhood, each pixel belonging to S_{void} is programmed to compare with its eight adjacencies based on the value of r_i. Consequently, the pixels occupying the centers of the porous body are collected and denoted as S_{pore}.

4) Obtaining a skeleton based on the grassfire algorithm. A fundamental aspect of the grassfire algorithm is outside-in-oriented deletion of pixels in S_{void}, where the topological properties of the porous structure are invariant; that is, the number of pixels in S_{void} does not change. To execute the deletion, we defined a new variable d_i, $d_i \in Z^+$, which is expressed as $d_i = \{r^2 | 1 \le i \le n\}$. If any r_i satisfies the condition of $r_i^2 = d_i$, the corresponding pixels belonging to S_{void} are reclassified to join S_{matrix} under the condition that S_{void} maintains its integrity. Accordingly, starting from $d_i = d_{\min} = 1$, the scope of S_{void} is decreased layer by layer with an increasing value of d_i. This process continues until only a single layer of pixels is left. It should be noted that bistratal pixels are still possible in specific localities where the value of r_i appears to be indistinctive for the two layers. The chain, composed of black pixels, is defined as the skeleton of the porous structure.

5) Realizing algorithms 1) through 4). To realize these algorithms, a program was written using the MATLAB platform. The calculated results were output in an image reflecting the actual morphology of the skeleton using black and white pixels. Furthermore, to directly visualize the value of r_i for each pixel, the skeleton was also shown in the form of an EXCEL table in which the grids symbolize the pixels of the image and are filled in corresponding to r_i. The columns and rows in the table are occupied in terms of the sheet format of the original image to illustrate the porous structure. Consequently, most of the grids are filled with zeros except where the substitutes of the pixels compose the skeleton of the porous structure.

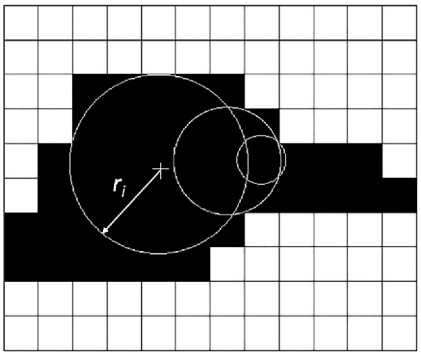

Figure 1 Schematic of a circle of black pixels, where one block represents a single pixel.

2.2 Determination of preferential flow paths

Based on the pore network model, a preferential path is determined by separating the paths of interest from the other paths, and then assigning a set of unique, compact numbers to them [48,49].

2.2.1 Definition of nodes based on pore network

A skeleton is a dendritic network composed of various branches. To construct a pore network, it is critical to make the intersection nodes connect to flow branches that are identifiable by a computer program. To achieve this task, we employed the following method to identify the nodes of the skeleton network. The intersections of the different branches and terminal points of the free end of any branch are both defined as nodes of the skeleton. Based on the fact that pores always connect with the throat and that the diameter of a pore is larger than that of the throat, the intersections in the skeleton must be at the centers of the pores. Furthermore, we numbered the sequences of points adjacent to one point in the image in the order shown in Figure 2. The intersections of the branches have the maximum corresponding radii (r_i), whereas the terminal points of the free end each have only one adjacent point belonging to the skeleton.

Two conditions must be met to define the nodes in the skeleton:

1) The current point is a skeleton point.

2) One of the following criteria is satisfied: another unique skeleton point can be found from its adjacent points; there are at least three skeleton points among the adjacent points, and the value of r_i of the current point is the largest.

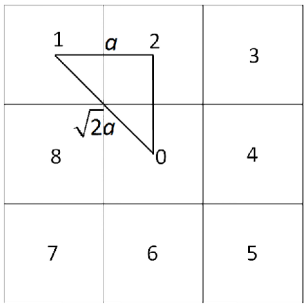

Figure 2 Numbering sequence of the adjacency of each pixel in the skeleton.

2.2.2 *Branches between nodes*

In addition to identifying nodes, the network model must also search the branches to calculate the flow path characteristics. With our procedure, the traveling graph is imported to ensure that all nodes of the skeleton are searched once. First, one of the entrance nodes is set as a starting point. Next, its eight adjacent points are searched in sequence from points 1 to 8, as shown in Figure 2. Once another point that belongs to the skeleton is observed, this point is defined as the new starting point for a continuous search to obtain the next skeleton point that has never been searched until a new node is acquired. Thus, the path between these two nodes is defined as a single branch. Furthermore, the last node is searched to determine whether another skeleton point exists at its adjacent position. If another skeleton point exists there, then the search process described above is repeated, and this node is taken as the starting point. Otherwise, the preceding step is repeated to recheck the nodes and search one by one until all nodes in the skeleton have been searched.

During the search process for a single branch, the values of the minimum corresponding radius r, the actual length L, and the linear length L_w are also obtained.

1) r: the radius of one branch. The radius is determined based on the minimum corresponding radius of pixels composing a single branch. We record the value of r_i of the current point; however, once a smaller r_i is obtained, the original value of r_i is replaced with the smaller one. The smallest r_i obtained is denoted as r.

2) L: the actual length of the branch. During the search process, if the next point required is at location 2, 4, 6, or 8 (as shown in Figure 2), then the length of the two points is recorded as a; if it is at location 1, 3, 5, or 7, then the length of the two points is recorded as $\sqrt{2}a$. The summation of points in one branch is the value of L.

(3) L_w: the linear distance from the starting node to the terminal node. In our program, the distance is replaced with the horizontal distance between two nodes.

2.2.3 *Determination of the preferential path*

We hypothesize that a preferential flow is attributed to the viscous forces, which are determined based on the difference in the water head from the inlet to the outlet. According to Poiseuille's law [50], each branch in the pore network is treated as a circular tube with different radii and tortuosity, and the conductivity of the tubes therefore presents significant heterogeneity characterized by flow resistance. The dendritic network model described in this paper forms a control flow graph (CFG), as shown in Figure 3, in which a weight is assigned to a single branch. This weight is characterized based on the flow resistance in the network model. With this knowledge, we calculated the shortest path in an undirected graph to determine the preferential flow in our network model because of the similar approach taken when applying the flow resistance as the weight of each branch.

We utilized Floyd's algorithm [51], which is a typical algorithm for calculating the shortest path because of its efficiency for both directed and undirected graphs. The set of branches with the smallest flow resistance is allowed to flow through and form a preferential path. The general idea of Floyd's algorithm is as follows:

1) Define the adjacency matrix $\boldsymbol{D}$ as $\boldsymbol{D}=\left[G_{ij}\right]_{n\times n}$, where $\boldsymbol{D}=\begin{cases}\omega_{ij}, & \text{if}(v_i,v_j)\in E,\\ \infty, & \text{otherwise,}\end{cases}$ in which E is the set of branches in the graph, and ω_{ij} is the weight of each branch, described as (v_i, v_j).

2) Update the value of ω_{ij} in matrix $\boldsymbol{D}$, a total of k=n times, where k is the number of updates, and n is the number of nodes, with the exception of nodes i and j.

(i) When k=0, $\boldsymbol{D}^{(0)}$=D.

(ii) Set k=k+1. Update $\boldsymbol{D}^{(k)}=\left(\omega_{ij}^{(k)}\right)_{n\times n}$, $k=1,2,...,n$, $\omega_{ij}^{(k)}=\min\left[\omega_{ij}^{(k-1)},\omega_{ik}^{(k-1)},\omega_{kj}^{(k-1)}\right]$, and record it as ω_{ik}+ω_{kj}=ω_{ikj}.

(iii) Until k=n, matrix $\boldsymbol{D}^{(n)}$ is the final result. The value of $\omega_{ij}^{(n)}$ in $\boldsymbol{D}^{(n)}$ refers to the distance of the shortest path between nodes i and j, and the path is recorded as ikj.

In the pore network model, weight ω_{ij} is replaced by G_{ij} and allocated to each branch. Here, G_{ij} is the flow resistance, which is unique for each branch, and is calculated as follows.

The single-phase flow in a porous medium is generally characterized based on Darcy's law:

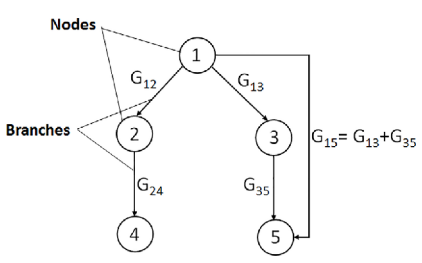

Figure 3 Schematic diagram of the network model.

$$Q = \frac{KA\Delta P}{\mu L}. \tag{3}$$

Thus,

$$\Delta P = \frac{\mu L}{KA} Q. \tag{4}$$

The flow flux Q is determined by $\frac{\mu L}{KA}$ under a certain pressure gradient ΔP in a tube. Therefore, let $G = \frac{\mu L}{KA}$, in which G is defined as the flow resistance. Here, μ is the viscosity of the fluid, and K is the permeability of the tube. In accordance with the Kozeny-Carman equation, K can be expressed as

$$K = \frac{1}{8\tau^2}\varphi r^2, \tag{5}$$

where φ is the porosity of the structure. For a circular tube, φ is equivalent to 1. In addition, τ is the tortuosity and is defined as $\tau = \left(\frac{L_w}{L}\right)^2$.

Thus, one obtains

$$G = \frac{8\mu L_w^4}{\pi r^4 L^3}. \tag{6}$$

In this case, the preferential path can be searched using Floyd's algorithm, and by treating the pore network as a CFG. Path *ikj* is the preferential path, and $G_{ij}^{(n)}$ is its total flow resistance. The algorithms and principles were programmed using the C++ language following the flow diagram in Figure 4, and encapsulated into software [52].

3 Examples

A previously developed porous structure and studies conducted by Keller et al. [53] and Sirivithayapakorn et al. [54] were employed herein. This porous structure was obtained from a thin slice of Berea sandstone observed through an optical microscope (approximately 600 μm×600 μm) and slightly modified to improve connectivity. To analyze the porous structure numerically, the image was processed into a binary image based on a self-developed image processing program [55,56]. Figure 5 shows a processed image of the porous structure, which is composed of white and black pixels. The white pixels represent homogeneous matrix, and the black pixels represent continuous pores and throats.

Figure 6 shows the topological skeleton network of this porous structure. Consequently, a total of 96 nodes in the skeleton were searched by the program and numbered consecutively in the order that they were searched within the image. The results are shown in Figure 7. Based on comparison of the skeleton figure with the original, nodes 29, 55, 77, and 94 were defined as the entrance of the pore network

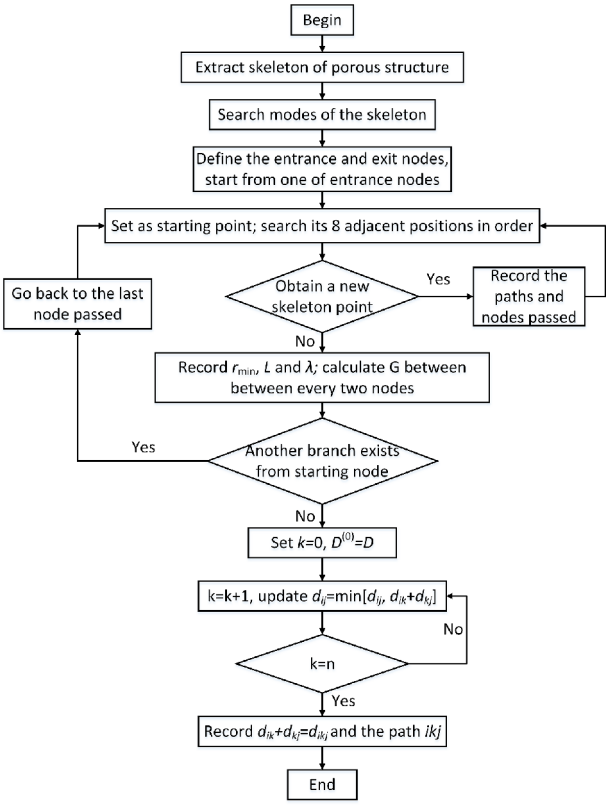

Figure 4 Flow diagram of the computing program for preferential flow paths.

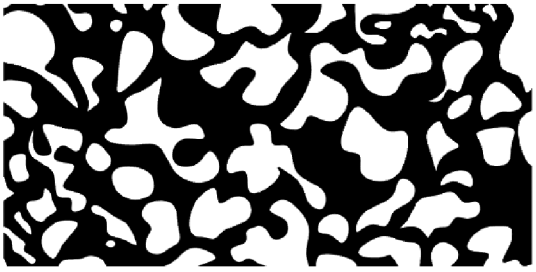

Figure 5 Original image of the porous structure (the black areas are pores, and the white areas are the matrix).

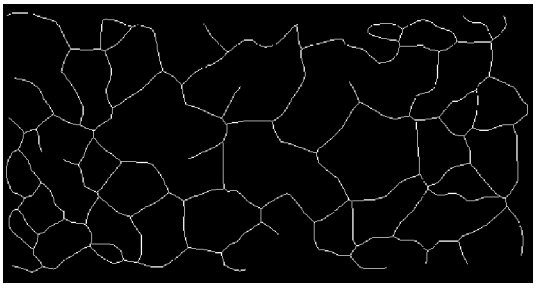

Figure 6 Topological skeleton network of the porous structure shown in Figure 5 (the white line indicates the morphology of the skeleton).

model, whereas node 88 was the exit. Furthermore, the preferential paths were calculated from the entrance to the exit as follows:

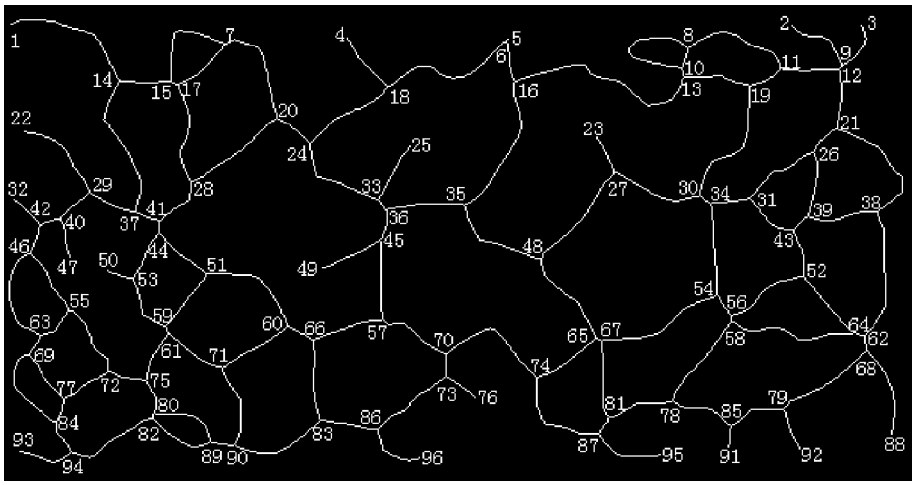

Figure 7 Node distribution in the skeleton network.

1) The paths between any two nodes were searched, and the seepage resistance G was then calculated. Water was considered a penetrative fluid with a viscosity of 1×10^3 Pa s.

2) The preferential paths from the entrance to the exit were explored.

The calculation results are given in Table 1. It is clear that the total seepage resistance of path ① was close to that of path ② but smaller than that of paths ③ and ④. Therefore, paths ① and ② were the preferential paths in this porous structure, and are indicated with a light green color in the skeleton figure shown in Figure 8.

4 Experimental validation of water flow in a heterogeneous porous medium

4.1 Perspex sheet model

For comparison, the porous structure used was machined onto a Perspex sheet using highly accurate machine tools. The Perspex sheet was transparent and enabled the flow process to be directly recorded using a high-definition camera. Figure 9 shows the ablated transparent model in which the pore size was expanded to millimeter scale to make it easier to observe the flow process. Moreover, we glued another, thinner Perspex sheet onto the surface of the etched plane to seal the porous model and make it more difficult for water to penetrate the interface of the two Perspex sheets. Figure 9 demonstrates the prepared experimental model with a geometry of 240 mm×120 mm. In addition, a Perspex water tank was designed to connect with the model, as shown in Figure 10. During the experiment, water was injected into the tank through a tube fixed to the side wall. For comparison, the water heads were set at three different levels (1, 2 and 4 cm) to provide different pressure gradient scenarios. Note that water pressure decreased as the water head advanced within the porous structure. Consequently, the pressure gradient became variable and disobeyed the assumption of our model. Thus, injection into the tank continued throughout the entire experiment, and a series of circular holes were punched into another side of the tank at different heights for drainage to ensure that the water mass was maintained at the presupposed height. Because three water head heights were used in this study, the holes below the water level were sealed with glue to prevent water leakage when higher water heights were used. Thus, a stable water pressure gradient was achieved from the inlet to the outlet during the experiments.

4.2 Experimental procedures and measurements

To increase the contrast of the fluid trajectory with the pore matrix, ink-dyed water (a mixture of red ink and water at a weight ratio of 3%) was used for the wetting phase. The influence of the tracer transport on fluid flow was negligible for the small dosage used. During the experiment, the red solution was first injected at the target height, and the sluice was lifted to release the fluid into the porous model. Thus, the entire inlet would have equal opportunity to meet the fluid body. Because the pore space was saturated with air until water invasion, this experiment was a process of imbibition, whereby the wetting water phase displaced the non-wetting air initially present in the heterogeneous porous medium. A high-speed camera fixed above the transparent sheet recorded the entire flow process for in-depth analysis.

4.3 Experimental results and discussion

Figure 11 illustrates the advancement of the water front over time. Figure 11(a) and (b) shows different instances of the entire flow process at the water heights of 1 and 2 cm with 1-

Table 1 Calculated results of the preferential path from the entrance to the exit

Number	Entrance to exit	Number of nodes in the preferential path	Total flow resistance (Pa s/mm^2)
1	29→88	29→37→41→28→20→24→33→36→35→48→65→74→87→81→78→85→79→68→88	5.327×10^4
2	77→88	77→72→75→80→82→89→90→83→86→73→70→74→87→81→78→85→79→68→88	5.618×10^4
3	94→88	94→84→77→72→75→80→82→89→90→83→86→73→70→74→87→81→78→85→79→68→88	6.567×10^4
4	55→88	55→63→69→77→72→75→80→82→89→90→83→86→73→70→74→87→81→78→85→79→68→88	6.994×10^4

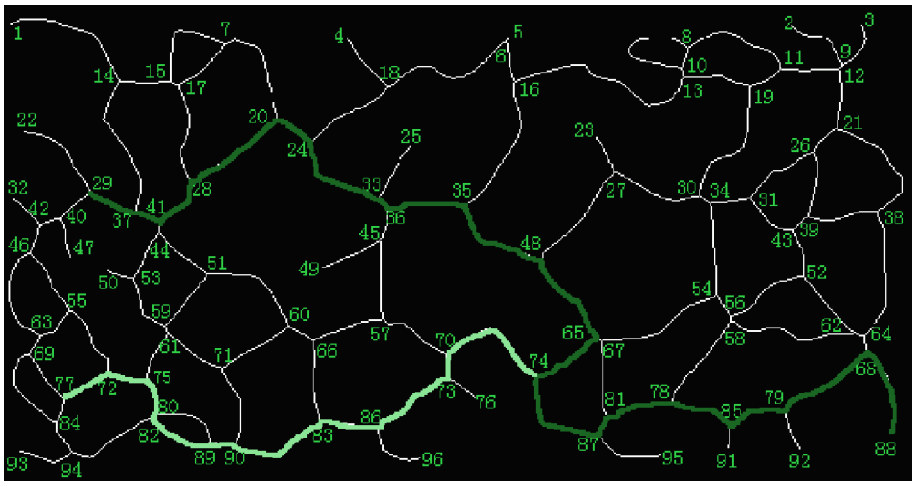

Figure 8 Preferential flow paths in the skeleton network (the line highlighted in darker dark green is path ①, and the line highlighted in light green indicates path ②).

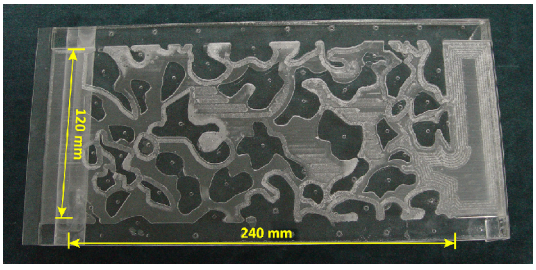

Figure 9 2D ablated porous structure of a Perspex sheet.

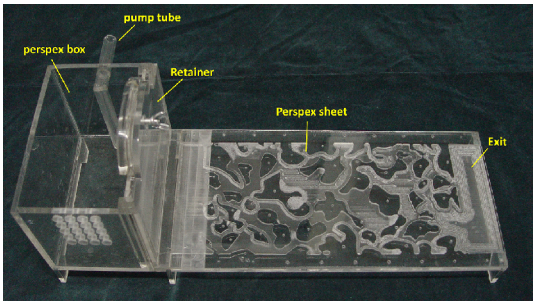

Figure 10 Assembled testing system composed of the water tank and Perspex sheets.

sintervals, compared with the 0.5-s time intervals for the images in Figure 11(c), which illustrates the fluid dynamic at the water height of 4 cm. The replications showed that preferential flow appeared to occur in the well-connected porous structure, and coincided with the analytical prediction of the proposed model for all cases. Moreover, to strength the analysis of the imbibitional preferential flow during the displacement of air by water, we calculated the water imbibition time of each case and plotted the results in Figure 12. The results show that water displaces air from inlet to outlet in about 8 s when water height is 1 cm, which is much longer than the imbibition time (5 s) when the water height is 2 cm, and approximately three times longer than that when the water height is 4 cm. The volume of the imbibed water is proportional to the square root of the imbibition time, which follows Handy's equation in water-air imbibition [57]. Nevertheless, the final imbibed volume of water according to the model when water height is 4 cm is slightly lower than that of the other two cases. This difference is because large air bubbles were trapped in the fluid body during the imbibition process at the highest water height, as illustrated in Figure 11(c), which rarely occurred in the other two cases.

Previous studies have shown that pore geometry determines which imbibition mechanisms occur [58,59]. Based

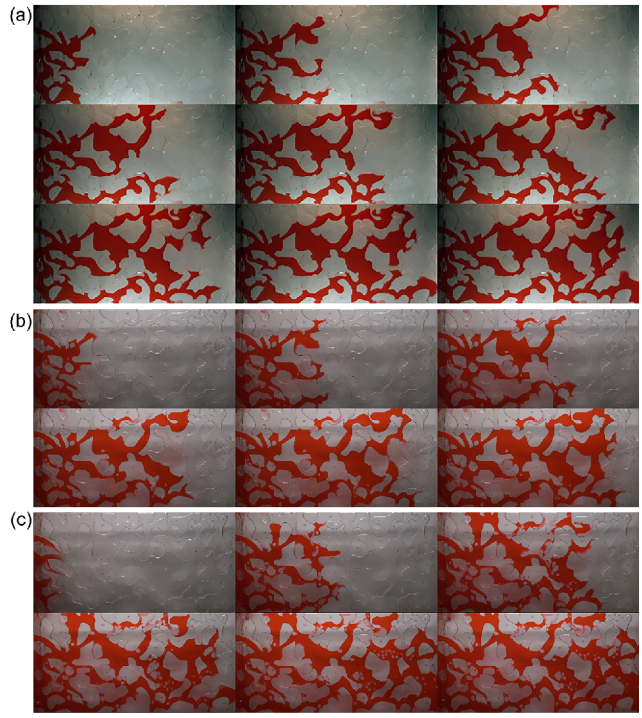

Figure 11 Time-lapse fluid dynamics in a heterogeneous porous structure. (a)–(c) Instances of fluid trajectories at the water heights of 1, 2 and 4 cm, respectively. The red flow lines indicate the saturated pores and throats during water front advancement.

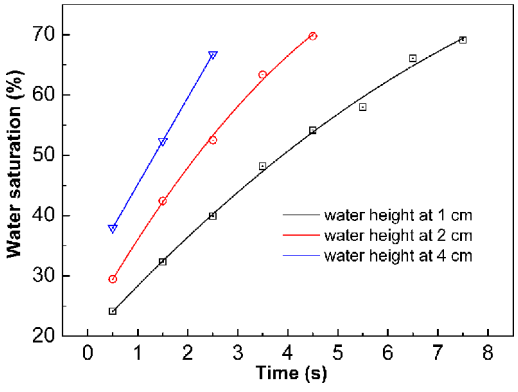

Figure 12 Water saturation during the invasion at different water height.

on previously proposed classification methods [59–61] and the test results of this study, we classified three types of imbibition mechanisms that occur during the water invasion process: piston-type invasion, tortuous throat flow, and macropore filling.

1) Piston-type invasion. Piston-type invasion occurs in narrow throats with a lower tortuosity; in this case, the throats are invaded by fluid occupying the bulk of the pore space containing no air bubbles on the fluid front. In addition, preferential flow can hardly be seen (Figure 13(a)).

2) Tortuous throat flow. When the fluid bypasses a tortuous throat, the fluid bulk can no longer cover the throat space, but instead advances in a thin film. Behind the front, although the following fluid bulk attempts to saturate the residual spaces, air residing in the corners easily traps the phase to form isolated clusters within the narrow pore throats, particularly when the tortuosity varies drastically (Figure 13(b)).

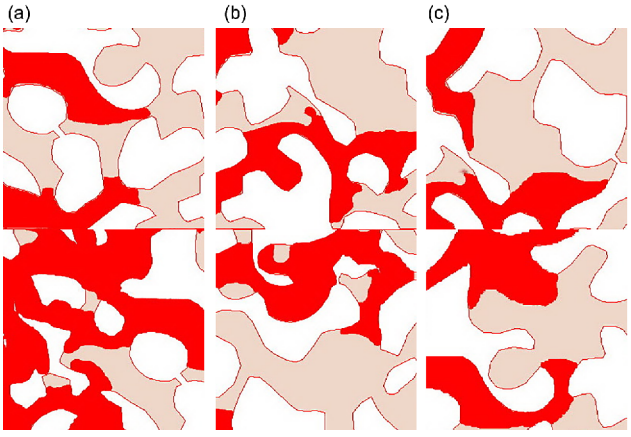

Figure 13 Fluid dynamics for typical pore geometries. (a) Piston-like flow in low-tortuosity throats; (b) fluid flow bypassing high-tortuosity paths; (c) fluid filling in macropores.

3) Macropore filling. When the water head enters the macropores, the pores cannot be invaded by piston-type displacement; instead, the water preferentially flows along the wall of the porous body until it fully fills in the pore space over time (Figure 13(c)). Moreover, the filling of the pores depends not only on the size of the porous body, but also on the number of adjacent throats that have already been filled with water. Thus, preferential flow strongly depends on the orientation, continuity, and cluster distribution of the macropores.

4.4 Comparison of theoretical and experimental results

Because the flow pattern during the imbibition process is similar at different water heights, we selected only the experimental results at the water height of 1 cm to compare with the calculated results. In Figure 14, a map of the porous skeleton obtained using our model was placed on the surface of the porous structure. In addition, the preferential paths calculated from the defined entrance to the exit were dyed for comparison with the experiment results.

The red solution entered the entrances uniformly during the early stage, as shown in Figure 14(a) and (b). However, three flow paths exceeded other fluid peaks, beginning with the image shown in Figure 14(c). Furthermore, the fluid tended to fill in the macropores, as shown in Figure 14(d) and (e). Two paths converged and saturated the macropores before continuing to flow forward. A similar phenomenon is shown in Figure 14(f) and (g), in which the paths converged at other macropores. Note that the fluid initiated and deviated

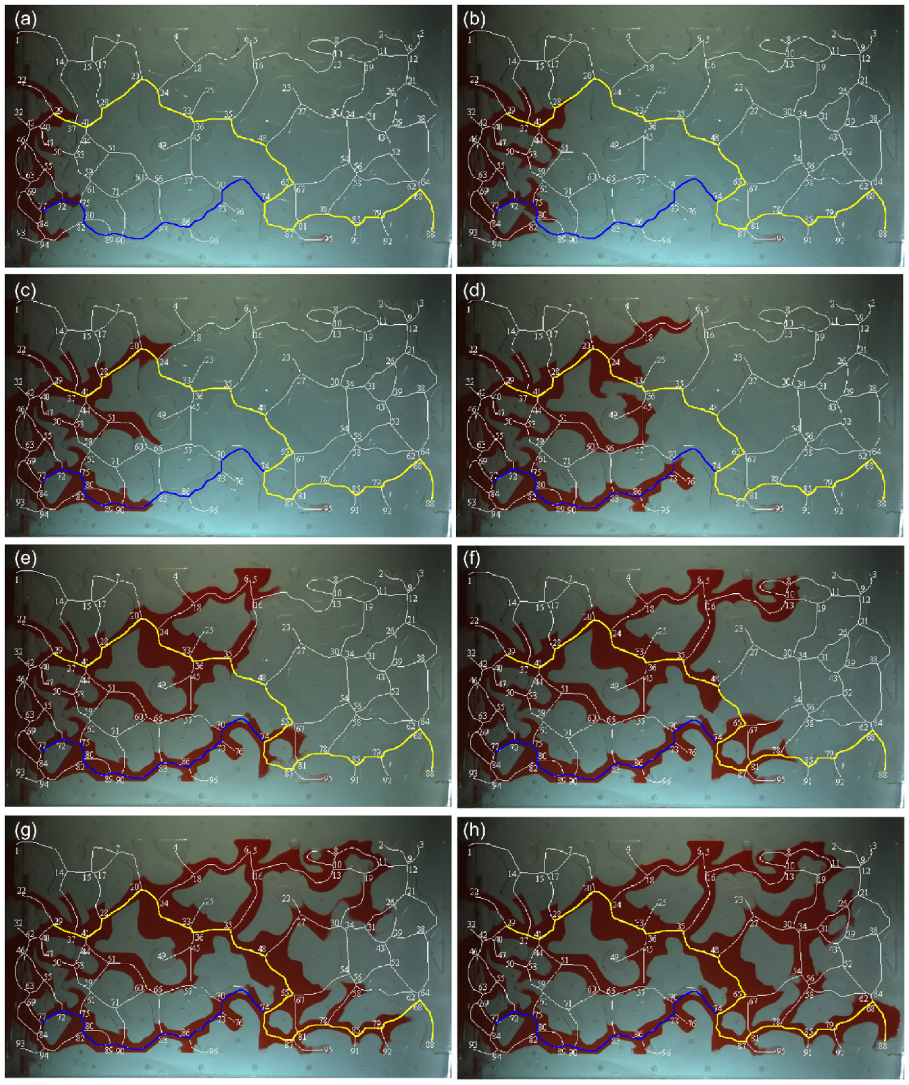

Figure 14 Comparison of the experimental and predicted results (development of a fluid peak over time is shown in (a) through (h)).

from the theoretical preferential path after the macropores were filled. However, these paths eventually arrived at another exit in addition to the defined exit. In other words, more preferential paths can be obtained through our model if more possible exits are defined.

5 Conclusions

A simple algorithm and computer program were developed to predict preferential flow paths based on the topological network model and the flow resistance of a porous structure, instead of on the flow behavior of the fluid. The algorithm simplifies a porous system into circular tubes in series or in parallel based on Poiseuille's law. The preferential paths are selected by calculating the flow resistance of the branches, which represents the flow capacity of the flow paths. Note that the algorithm was developed under the condition that the pore space is composed of connected macropores, and that the effects of fluid properties are negligible. The algorithm focuses on the plot and profile scale based on graph theory. Therefore, the model has certain limitations. However, the method accurately predicts a preferential path based on an accurate porous model. The efficiency of the algorithm was verified through comparison between analytical and experimental results. The predicted results were tested using the same porous structure ablated on a Perspex sheet. The comparison indicates that the predicted results fit well with the experimental results.

It should be noted that in our simple model, the wettability is assumed to be constant and uniformly distributed through the entire porous structure. In reality, the preferential flow pattern of two-phase imbibition in a complex porous system could be influenced by multiple factors including the nature

of the fluid, the characteristics of the structure, and interaction between the structure and fluid. To address our primary objective, our model only takes into account the influence of structural irregularity on preferential flow.

This work was supported by the National Natural Science Foundation of China (Grants Nos. 51374213, 51674251 & 51727807), the State Key Research Development Program of China (Grant No. 2016YFC0600705), the National Natural Science Fund for Distinguished Young Scholars (Grant No. 51125017), the Fund for Creative Research and Development Group Program of Jiangsu Province (2014-27), and the Priority Academic Program Development of Jiangsu Higher Education Institutions (Grant No. PAPD-2014).

1 Šimůnek J, Jarvis N J, van Genuchten M T, et al. Review and comparison of models for describing non-equilibrium and preferential flow and transport in the vadose zone. J Hydrol, 2003, 272: 14–35
2 Zhang Y, Yao F, Xu D, et al. Stochastic simulation on preferential seepage channels in water-flooding reservoirs. Electron J Geotech Eng, 2015, 20: 803–812
3 Birk S, Liedl R, Sauter M. Karst spring responses examined by process-based modeling. Groundwater, 2006, 44: 832–836
4 Sinkevich M G, Walter M T, Lembo A J, et al. A GIS-based ground water contamination risk assessment tool for pesticides. Ground Water Monit Rem, 2005, 25: 82–91
5 Wang Z, Jury W A, Tuli A, et al. Unstable flow during redistribution. Vadose Zone J, 2004, 3: 549–559
6 Gomez H, Cueto-Felgueroso L, Juanes R. Three-dimensional simulation of unstable gravity-driven infiltration of water into a porous medium. J Comp Phys, 2013, 238: 217–239
7 Beven K, Germann P. Macropores and water flow in soils revisited. Water Resour Res, 2013, 49: 3071–3092
8 Jarvis N J. A review of non-equilibrium water flow and solute transport in soil macropores: Principles, controlling factors and consequences for water quality. Eur J Soil Sci, 2007, 58: 523–546
9 Armstrong R T, Berg S. Interfacial velocities and capillary pressure gradients during Haines jumps. Phys Rev E, 2013, 88: 600–614
10 Armstrong R T, Evseev N, Koroteev D, et al. Modeling the velocity field during Haines jumps in porous media. Adv Water Resour, 2015, 77: 57–68
11 Kazemifar F, Blois G, Kyritsis D C, et al. Quantifying the flow dynamics of supercritical CO_2-water displacement in a 2D porous micromodel using fluorescent microscopy and microscopic PIV. Adv Water Resour, 2015, 95: 352–368
12 Kazemifar F, Blois G, Kyritsis D C, et al. A methodology for velocity field measurement in multiphase high-pressure flow of CO_2 and water in micromodels. Water Resour Res, 2015, 51: 3017–3029
13 Wehrer M, Slater L D. Characterization of water content dynamics and tracer breakthrough by 3-D electrical resistivity tomography (ERT) under transient unsaturated conditions. Water Resour Res, 2015, 51: 97–124
14 Berg S, Ott H, Klapp S A, et al. Real-time 3D imaging of Haines jumps in porous media flow. Proc Natl Acad Sci USA, 2013, 110: 3755–3759
15 Herring A L, Andersson L, Schlüter S, et al. Efficiently engineering pore-scale processes: The role of force dominance and topology during nonwetting phase trapping in porous media. Adv Water Resour, 2015, 79: 91–102
16 Ptak T, Piepenbrink M, Martac E. Tracer tests for the investigation of heterogeneous porous media and stochastic modelling of flow and transport—A review of some recent developments. J Hydrol, 2004, 294: 122–163
17 Amidu S A, Dunbar J A. Geoelectric studies of seasonal wetting and drying of a texas vertisol. Vadose Zone J, 2007, 6: 511
18 Cuthbert M O, Mackay R, Tellam J H, et al. The use of electrical resistivity tomography in deriving local-scale models of recharge through superficial deposits. Q J Eng Geol Hydrogeol, 2009, 42: 199–209
19 French H, Binley A. Snowmelt infiltration: Monitoring temporal and spatial variability using time-lapse electrical resistivity. J Hydrol, 2004, 297: 174–186
20 Garré S, Koestel J, Günther T, et al. Comparison of heterogeneous transport processes observed with electrical resistivity tomography in two soils. Vadose Zone J, 2010, 9: 336–349
21 Seven K, Germann P. Water flow in soil macropores II. A combined flow model. Can J Soil Sci, 1981, 32: 15–29
22 Beven K. Micro-, meso-, macroporosity and channeling flow phenomena in soils. Soil Sci Soc Am J, 1981, 45: 1245
23 Beven K, Germann P. Macropores and water flow in soils. Water Resour Res, 1982, 18: 1311–1325
24 Skopp J. Comment on "micro-, meso-, and macroporosity of soil". Soil Sci Soc Am J, 1981, 45: 1246
25 Blunt M J, Bijeljic B, Dong H, et al. Pore-scale imaging and modelling. Adv Water Resour, 2013, 51: 197–216
26 Wildenschild D, Sheppard A P. X-ray imaging and analysis techniques for quantifying pore-scale structure and processes in subsurface porous medium systems. Adv Water Resour, 2013, 51: 217–246
27 Nejad Ebrahimi A, Jamshidi S, Iglauer S, et al. Genetic algorithm-based pore network extraction from micro-computed tomography images. Chem Eng Sci, 2013, 92: 157–166
28 Coon E T, Porter M L, Kang Q. Taxila LBM: A parallel, modular lattice Boltzmann framework for simulating pore-scale flow in porous media. Comput Geosci, 2014, 18: 17–27
29 Muljadi B P, Blunt M J, Raeini A Q, et al. The impact of porous media heterogeneity on non-Darcy flow behaviour from pore-scale simulation. Adv Water Resour, 2016, 95: 329–340
30 Al-Raoush R, Thompson K, Willson C S. Comparison of network generation techniques for unconsolidated porous media. Soil Sci Soc Am J, 2003, 67: 1687–1700
31 Al-Raoush R I, Willson C S. Extraction of physically realistic pore network properties from three-dimensional synchrotron X-ray microtomography images of unconsolidated porous media systems. J Hydrol, 2005, 300: 44–64
32 Lindquist W B, Lee S M, Coker D A, et al. Medial axis analysis of void structure in three-dimensional tomographic images of porous media. J Geophys Res, 1978, 101: 8297–8310
33 Nolan G T, Kavanagh P E. Computer simulation of random packing of hard spheres. Powder Tech, 1992, 72: 149–155
34 Vogel H J. Topological characterization of porous media. In: Mecke K, Stoyan D, Eds. Morphology of Condensed Matter-Physics and Geometry of Spatially Complex Systems. Berlin Heidelberg: Springer Press, 2002. 75–92
35 Vogel H J, Roth K. Quantitative morphology and network representation of soil pore structure. Adv Water Resour, 2001, 24: 233–242
36 Vogel H J, Roth K. Moving through scales of flow and transport in soil. J Hydrol, 2003, 272: 95–106
37 Vogel H J, Cousin I, Ippisch O, et al. The dominant role of structure for solute transport in soil: Experimental evidence and modelling of structure and transport in a field experiment. Hydrol Earth Syst Sci, 2005, 10: 495–506
38 Deurer M, Green S R, Clothier B E, et al. Drainage networks in soils. A concept to describe bypass-flow pathways. J Hydrol, 2003, 272: 148–162
39 Yang G, Cook N G W, Myer L R. Analysis of preferential flow paths using graph theory. Int J Rock Mech Min Sci Geomech Abstr, 1993, 30: 1423–1429
40 Gwo J P. In search of preferential flow paths in structured porous media using a simple genetic algorithm. Water Resour Res, 2001, 37: 1589–1601

41 Mason G, Morrow N R. Capillary behavior of a perfectly wetting liquid in irregular triangular tubes. J Colloid Interface Sci, 1991, 141: 262–274
42 Wong P Z, Koplik J, Tomanic J P. Conductivity and permeability of rocks. Phys Rev B, 1984, 30: 6606–6614
43 Dong H, Blunt M J. Pore-network extraction from micro-computerized-tomography images. Phys Rev E, 2009, 80: 1957–1974
44 Silin D B, Jin G, Patzek T W. Robust determination of the pore space morphology in sedimentary rocks. In: SPE Annual Technical Conference and Exhibition. Denver, Colorado, 2003
45 Blum H. A transformation for extracting new descriptors of shape. In: Wathen-Dunn W, Ed. Models for the Perception of Speech & Visual Form. Amsterdam: MIT Press, 1967. 362–380
46 Baldwin C A, Sederman A J, Mantle M D, et al. Determination and characterization of the structure of a pore space from 3D volume images. J Colloid Interface Sci, 1996, 181: 79–92
47 Silin D, Patzek T. Pore space morphology analysis using maximal inscribed spheres. Physica A, 2006, 371: 336–360
48 Vaswani K, Nori A V, Chilimbi T M. Preferential path profiling. SIGPLAN Not, 2007, 42: 351–362
49 Li B, Wang L, Leung H, et al. Profiling all paths: A new profiling technique for both cyclic and acyclic paths. J Syst Software, 2012, 85: 1558–1576
50 Adler P. Porous Media: Geometry and Transports. Boston: Elsevier, 2013
51 Floyd RW. Algorithm 97: Shortest path. Communications of the ACM, 1969. 345
52 Ju Y Liu P, Yang Y, et al. Software of seepage network model and preferential flow analysis in porous media (in Chinese). Software Copyright Registration, CUMTB, Beijing, 081126, 2012
53 Keller A A, Blunt M J, Roberts A P V. Micromodel observation of the role of oil layers in three-phase flow. Transp Porous Media, 1997, 26: 277–297
54 Sirivithayapakorn S, Keller A. Transport of colloids in saturated porous media: A pore-scale observation of the size exclusion effect and colloid acceleration. Water Resour Res, 2003, 39: SBH111
55 Ju Y, Xing M, Sun H. Computer program for extracting and analyzing fractures in rocks and concretes (in Chinese). Software Copyright Registration, CUMTB, Beijing, 0530646, 2013
56 Ju Y, Zheng J, Epstein M, et al. 3D numerical reconstruction of well-connected porous structure of rock using fractal algorithms. Comput Methods Appl Mech Eng, 2014, 279: 212–226
57 Handy L L. Determination of effective capillary pressures for porous media from imbibition data. Pet Trans, 1960, AIME 219: 75–80
58 Patzek T W. Verification of a complete pore network simulator of drainage and imbibition. SPE J, 2001, 6: 144–156
59 Wang S, Feng Q, Dong Y, et al. A dynamic pore-scale network model for two-phase imbibition. J Nat Gas Sci Eng, 2015, 26: 118–129
60 Nguyen V H, Sheppard A P, Knackstedt M A, et al. The effect of displacement rate on imbibition relative permeability and residual saturation. J Pet Sci Eng, 2006, 52: 54–70
61 Lenormand R, Zarcone C, Sarr A. Mechanisms of the displacement of one fluid by another in a network of capillary ducts. J Fluid Mech, 1983, 135: 337–353